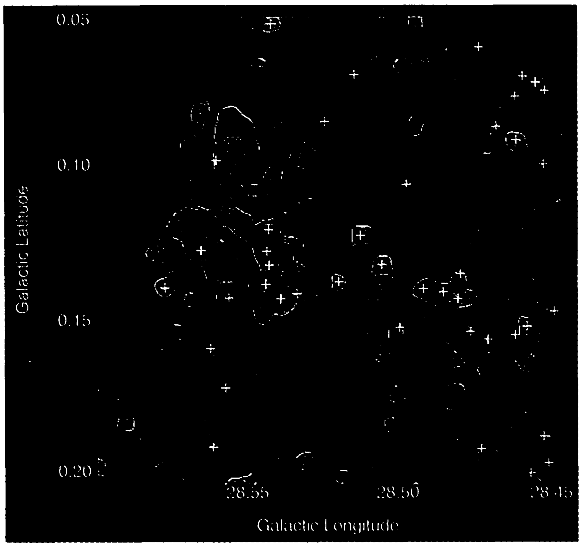

Fig. 3. Close-up of the diffuse feature at around (*l*,*b*) ≈ (28°.55,−0°.12). The 0.5- to 3-keV image is represented in red, the 3- to 8-keV image is in blue, and both images are smoothed to enhance the diffuse feature. A contour map of the 3- to 8-keV image is superimposed. Point sources detected with more than 3σ confidence either in the 0.5- to 3-keV band or the 3- to 8-keV band are indicated with crosses. The image is 560 pixels by 560 pixels with the pixel size 0.″98 square.

quiescent dwarf nova population. For example, a combination of a 10^{-5} pc^{-3} spatial density and 10^{31} erg s^{-1} average luminosity of quiescent dwarf novae, which amounts to ~1000 sources/degree^2 at $>3 \times 10^{-15}$ ergs s^{-1} cm^{-2} (*9*), is clearly ruled out. To be consistent with our observation, either spatial density or average luminosity has to be smaller at least by a factor of 4.

The paucity of Galactic point sources supports models of diffuse emission to explain the Galactic ridge x-ray emission. Then, the next question is how to produce plasmas with such a large energy density and high temperatures, and keep them in the Galactic disk. Theories have been proposed to explain these problems in terms of interstellar-magnetic reconnection (*13*), or interaction of energetic cosmic-ray electrons (*14*) or heavy ions (*15*) with interstellar medium. All of these models require supernovae as a mechanism of the energy input. Incidentally, in the region around (*l*,*b*) ≈ (28°.55,–0°.12), we found an extended feature with a size of ~2′, which is more conspicuous in the hard x-ray band than in the soft band (Fig. 3). This region corresponds to the southern end of an extended and patchy radio source named G28.60-0.13 (*16*), and the diffuse x-ray structure we found bridges three discrete radio patches: F, G, and H (*16*). A high-quality x-ray spectrum of the G28.60-0.13 region by the ASCA satellite indicates that the energy spectrum is a single power law without any iron line emissions (*17*), reminiscent of the nonthermal acceleration taking place in the supernova remnants suchas SN1006 (*18*) or RX J1713.7-3946 (*19*).The extended feature at (*l*,*b*) ≈(28°.55, −0°.12), or G28.60-0.13 itself, may be an aged supernova remnant. Supernova remnants may be ubiquitous on the Galactic plane (*16*), and these remnants may have an important role in generating the Galactic ridge hard x-ray emission (*20*).

References and Notes

1. K. Koyama *et al.*, *Publ. Astron. Soc. Jpn.* **38**, 121 (1986).
2. R. S. Warwick, M. J. L. Turner, M. G. Watson, R. Wilingale, *Nature* **317**, 218 (1985).
3. H. Kaneda *et al.*, *Astrophys. J.* **491**, 638 (1997).
4. D. M. Worrall, F. E. Marshall, E. A. Boldt, J. H. Swank, *Astrophys. J.* **255**, 111 (1982).
5. K. Mukai, K. Shiokawa, *Astrophys. J.* **418**, 863 (1993).
6. R. Ottmann, J. H. M. M. Schmitt, *Astron. Astrophys.* **256**, 421 (1992).
7. M. G. Watson, in *Annapolis Workshop on Magnetic Cataclysmic Variable*, ASP Conference Series, vol. 157, C. Hellier, K. Mukai, Eds. (Astronomical Society of the Pacific, San Francisco, 1999), p. 291.
8. M. Sugizaki *et al.*, *Astrophys. J. Suppl.* **134**, 77 (2001).
9. S. Yamauchi *et al.*, *Publ. Astron. Soc. Jpn.* **48**, L15 (1996).
10. J. M. Dickey, F. J. Lockman, *Annu. Rev. Astron. Astrophys.* **28**, 215 (1990).
11. T. M. Dame, D. Hartmann, P. Thaddeus, *Astrophys. J.* **547**, 792 (2001).
12. R. Giacconi *et al.*, *Astrophys. J.* **551**, 624 (2001).
13. S. Tanuma *et al.*, *Publ. Astron. Soc. Jpn.* **51**, 161 (1999).
14. A. Valinia *et al.*, *Astrophys. J.* **543**, 733 (2000).
15. Y. Tanaka, T. Miyaji, G. Hasinger, *Astron. Nachr.* **320**, 181 (1999).
16. D. J. Helfand, T. Velusamy, R. H. Becker, F. J. Lockman, *Astrophys. J.* **341**, 151 (1989).
17. A. Bamba *et al.*, *Publ. Astron. Soc. Jpn.* **53**, accepted (2001).
18. K. Koyama *et al.*, *Nature* **378**, 255 (1995).
19. K. Koyama *et al.*, *Publ. Astron. Soc. Jpn.* **49**, L7 (1997).
20. K. Koyama, S. Ikeuchi, K. Tomisaka, *Publ. Astron. Soc. Jpn.* **38**, 503 (1986).
21. Y. Ueda *et al.*, *Astrophys. J.* **518**, 656 (1999).
22. We are grateful to F. E. Marshall, K. Mukai, and R. F. Mushotzky for helpful comments that improved an earlier version of this report. We also thank Y. Tanaka and other anonymous referees for useful comments. The observation was carried out under NASA's Chandra Guest Observer Program.

18 June 2001; accepted 30 July 2001
Published online 9 August 2001;
10.1126/science.1063529
Include this information when citing this paper.

Spatiotemporal Self-Organization in a Surface Reaction: From the Atomic to the Mesoscopic Scale

C. Sachs, M. Hildebrand, S. Völkening, J. Wintterlin,* G. Ertl

Scanning tunneling microscopy data revealed the atomic processes in propagating reaction fronts that occur in the catalytic oxidation of hydrogen on Pt(111). The fronts were also characterized on mesoscopic length scales with respect to their velocity and width. Simulations on the basis of a reaction-diffusion model reproduce the experimental findings qualitatively well. The quantitative comparison reveals the limitations of this traditional approach to modeling spatiotemporal pattern formation in nonlinear dynamics.

Spatiotemporal pattern formation in open systems far from equilibrium is the basis of self-organization of matter. Catalytic reactions between small molecules on well-defined solid surfaces are probably the simplest model systems that show such phenomena (*1*). Concentration patterns are formed on mesoscopic length scales (typically 1 μm to 1 mm) that can be imaged with techniques such as photoemission electron microscopy (*2*). Nonequilibrium patterns can be observed if the reaction kinetics fulfill certain criteria. The minimum requirements are the presence of nonlinearities and of spatial coupling. These patterns can be modeled with reaction-diffusion (RD) equations (*3, 4*), in which the properties of the individual particles are replaced by continuum variables such as adsorbate concentrations, and this approach often provides a good qualitative description. Fluctuations are usually neglected because the atomic scale (<1 nm) is much smaller than the typical length scale of the observed patterns.

Fritz-Haber-Institut der Max-Planck-Gesellschaft, D-14195 Berlin, Germany.

*To whom correspondence should be addressed. E-mail: wintterlin@fhi-berlin.mpg.de

However, effects on microscopic scales, such as lateral interactions between adsorbed particles, should affect the pattern formation. By tuning the scanning range in scanning tunneling microscopy (STM) experiments, both microscopic effects and the formation of mesoscopic patterns can be observed simultaneously. We have applied this technique to close the gap between atomic and mesoscopic length scales. During the catalytic oxidation of hydrogen on a Pt(111) surface, propagating reaction fronts evolve from the reacting surface species that are atomically resolved by STM. Theoretical modeling is performed on the basis of RD equations whose kinetic parameters were determined in independent experiments. The limitations of this approximation become evident when experimental and theoretical data are quantitatively compared.

The mechanism of the catalytic oxidation of H_2 to give water on a Pt(111) surface (ultrahigh vacuum conditions) has been previously explored (*5, 6*). The H_2 molecules adsorb dissociatively on the surface, which had been precovered with adsorbed oxygen atoms. Propagating reaction fronts were observed below the desorption temperature of H_2O (≈170 K), where an autocatalytic reaction sequence occurs

$$OH + H \xrightarrow{k_2} H_2O \qquad (II)$$

$$2\,H_2O + O \xrightarrow{k_3} 3\,OH + H \qquad (III)$$

The autocatalytic cycle is initiated by direct OH formation from the atomic adsorbates,

$$H + O \rightarrow OH \qquad (I)$$

which is a slow step under these conditions, or by adsorption of trace amounts of H_2O from the residual gas that enters step III. The 2:1 stoichiometry of H_2O and O in reaction III is based on evidence from experiments (*6, 7*) and from density functional theory (DFT) calculations (*8, 9*). The DFT calculations furthermore revealed low activation energies for steps II and III and a high value (~1 eV) for step I, in full agreement with this reaction sequence that leads to water formation at temperatures as low as 110 K (*10*).

Small-scale STM images (Fig. 1, A to C) show the reaction with atomic resolution. Adsorbed O atoms form an ordered (2 × 2)-overlayer on Pt(111). As the O layer was exposed to hydrogen, OH islands evolved (Fig. 1, A and B). Within the islands, strong attractive interactions act that are caused by hydrogen bonds between OH molecules (*6*). Closer inspection reveals that the OH patches completely fill the areas initially covered by oxygen. At first this fact appears surprising, because the OH phase has a density of oxygen species almost three times higher than the original (2 × 2)O structure. This local density increase is clearly not consistent with OH formation by step I, after which the density of oxygen species would have remained unchanged. However, the observation is in agreement with OH formation by step III. Water is mobile at these low temperatures, and it can travel into the scanned area by surface diffusion. Coupling of H_2O diffusion with reaction to give OH by step III can thus lead to a local density increase by a factor of 3. The source of the diffusing H_2O molecules becomes apparent from larger scale data (see below). When the OH phase almost covered the complete scanning area, H_2O islands developed that appear as fuzzy bright patches (Fig. 1C). The frizziness of the edges of these features is caused by the motion of water molecules during the STM scan and reflects the mobility of adsorbed H_2O at these temperatures.

STM images from larger surface areas (Fig. 1, D to F) revealed that the distribution of surface species—albeit starting from a uniform layer of adsorbed O and H—was by no means homogeneous during the reaction. The OH was largely concentrated in the bright ring that expanded as a reaction front into the oxygen-covered surface regions and left the reaction product water behind it. The H_2O islands that built up behind the front could be resolved in other experiments (*11*), in which, however, the OH in the front was less clearly visible. The accumulated H_2O behind the front was thus identified as the source of the diffusing H_2O molecules. The circular feature in the lower part of the images is a hole one Pt layer deep, which in this case acted as a nucleation center for the reaction front. However, during its further propagation, the reaction front passed across the monoatomic steps of the Pt surface (thin lines) without appreciable distortion. The modeling was therefore performed with a uniform surface. To start the reaction, an H_2O cluster was introduced as a nucleation center. In Fig. 1, A to C, the adsorbed particles did not display concentration gradients because of the small image size, and because the higher surface temperature (~20 K) than in Fig. 1, D to F, creates fronts about one order of magnitude wider.

The front position from Fig. 1, D to F, is a linear function of time (Fig. 2), so that the front velocity could be regarded as constant within experimental errors (15 ± 3 nm/min). The width of the front (Fig. 2B) remained unchanged during the experiment (~17 nm). Hence, the OH ring fulfills the two criteria, constant velocity and width, that are characteristic for propagating fronts in autocatalytic RD systems.

Modeling was performed within the

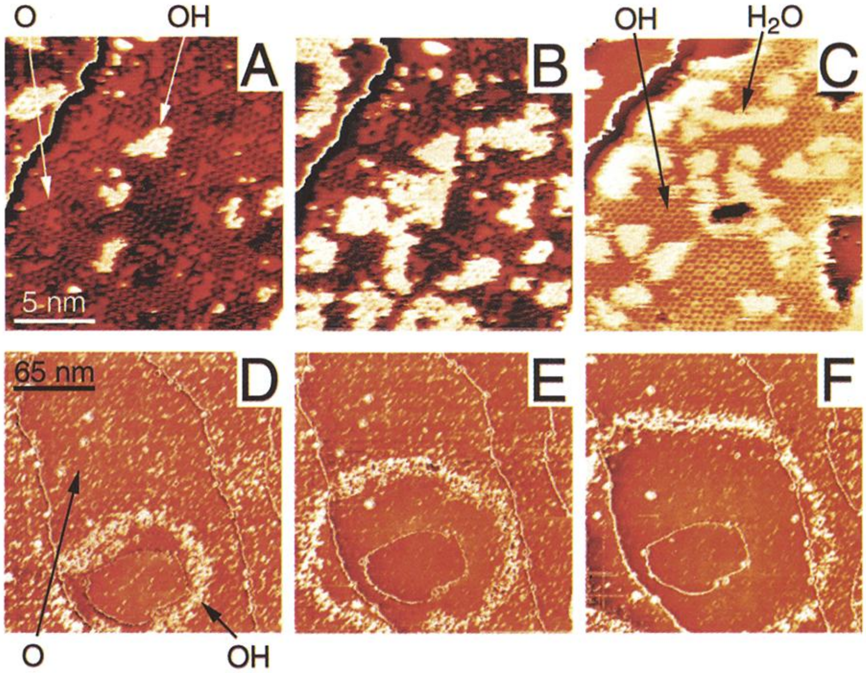

Fig. 1. Series of successive STM images, recorded during dosing of the O-covered Pt(111) surface with H_2. (**A** to **C**) Frames (17 nm by 17 nm) from an experiment at 131 K [$P(H_2) = 8 \times 10^{-9}$ mbar]. The hexagonal pattern in (A) is the (2 × 2)O structure; O atoms appear as dark dots and bright features are the initial OH islands. In (C), the area is mostly covered by OH, which forms ordered $(\sqrt{3}\times\sqrt{3})R30°$ and (3×3) structures. The white, fuzzy features are H_2O-covered areas. (**D** to **F**) Frames (220 nm by 220 nm) from an experiment at 112 K [$P(H_2) = 2 \times 10^{-8}$ mbar]. In (D), the surface is mostly O-covered (not resolved). The bright dots are small OH islands, most of which are concentrated in the expanding ring. H_2O in the interior of the ring is not resolved here. Thin, mostly vertical lines are atomic steps.

framework of RD equations, based on steps II and III. Step I is neglected because it is slow under the conditions considered (*9*). Step III is formulated as a second-order process based on previous kinetic measurements (*12*). Oxygen and OH are practically immobile at these temperatures, because of strong bonding to the surface and strong mutual attractive interactions. Adsorbed H atoms are so mobile that the H distribution can be regarded as spatially homogeneous. Hence, only the diffusion of adsorbed H_2O is included in the RD equations (concentrations of adsorbed species being marked by brackets)

$$\frac{\partial}{\partial t}[\mathrm{O}] = -k_3[\mathrm{H_2O}][\mathrm{O}] \qquad (1)$$

$$\frac{\partial}{\partial t}[\mathrm{H_2O}] = -2k_3[\mathrm{H_2O}][\mathrm{O}] + k_2[\mathrm{OH}][\mathrm{H}] + D\Delta[\mathrm{H_2O}] \qquad (2)$$

$$\frac{\partial}{\partial t}[\mathrm{OH}] = 3k_3[\mathrm{H_2O}][\mathrm{O}] - k_2[\mathrm{OH}][\mathrm{H}] \qquad (3)$$

Because hydrogen was continuously supplied from the gas phase, we can safely set $[H] = 1$.

The RD system of Eqs. 1 to 3 was solved by numerical integration of the two-dimensional (2D) system. From this analysis, the evolution of concentration profiles of adsorbed O, OH, and H_2O was obtained (Fig. 3). Initially, a nucleus of H_2O is surrounded by a uniformly O-covered surface, and the OH concentration is zero everywhere (frame 1 of the 1D cross sections). Water starts to diffuse into the O-covered area where it produces OH according to step III. The H_2O concentration in the nucleus decreases and an OH peak develops at the O/H_2O interface (frame 2). In frames 3 to 6, H_2O continuously diffuses from the interior region into the O-covered area where it reacts to form OH (step III), thereby driving the O/OH interface outward. Then, OH reacts with H to give H_2O (step II), causing the OH concentration to decrease again and the H_2O concentration to increase. The OH/H_2O interface thus follows the outward motion of the O/OH interface. As a result, a circular reaction zone that contains the OH moves through the O-covered area, thereby transforming the O into H_2O (2D frames). Diffusion of H_2O molecules from behind the front into the area ahead of the front thus explains the local density increase observed in the atomically resolved data during the OH formation. After the nucleation period, the front propagates with constant velocity and width. The RD model hence fully reproduces the qualitative characteristics of the experiment.

For a quantitative comparison with the experiment, the kinetic parameters of the RD system (k_2, k_3, D) were determined in independent experiments. The rate constant k_2 was determined by STM experiments in which, at first, an OH adlayer was prepared in the known way (*13*) by exposure of the O-covered surface to H_2O. Then, a constant H_2 pressure was adjusted to create a permanent supply of H atoms. The reaction of OH with H to give H_2O was monitored with the STM. If we assume that the H coverage is constant, then pseudo–first order rate constants $k_2 = 4.3 \times 10^{-4}\ \mathrm{ML}^{-1}\ \mathrm{s}^{-1}$ and $5.5 \times 10^{-3}\ \mathrm{ML}^{-1}\ \mathrm{s}^{-1}$ at 133 and 149 K, respectively, could be obtained (ML = monolayers). The corresponding Arrhenius parameters, $E_2 = 0.27$ eV and $\nu_2 = 8.7 \times 10^6\ \mathrm{ML}^{-1}\ \mathrm{s}^{-1}$, can be regarded as fairly rough estimates. Density functional theory (DFT) calculations revealed an activation energy $E_2 = 0.2$ eV (*9*), which is in reasonable agreement with the experimental value.

Time-resolved STM experiments to determine k_3 were not possible, because shielding effects prevented H_2O from adsorbing under the tip. Instead, a series of measurements by low-energy electron diffraction were performed. An O-covered surface was rapidly dosed with a stoichiometric quantity of H_2O, and the time-dependent decay of the (2×2)O spot intensity (proportional to the O-concentration) was recorded. The Arrhenius plot for the resulting k_3 data between 115 and 155 K yielded $E_3 = 0.20 \pm 0.09$ eV and $\nu_3 = 6 \times 10^{6\pm2.4}\ \mathrm{ML}^{-1}\ \mathrm{s}^{-1}$. The data are at significant variance with Arrhenius parameters ($E_3 = 0.44 \pm 0.03$ eV and $\nu_3 = 1.0 \times 10^{15\pm1.4}\ \mathrm{ML}^{-1}\ \mathrm{s}^{-1}$) determined previously by secondary ion mass spectroscopy (*12*). This difference is presumably due to the

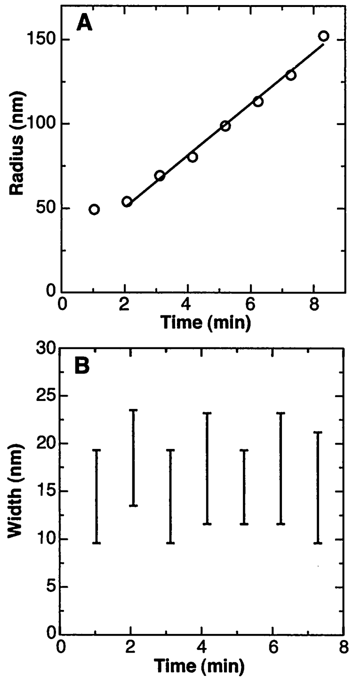

Fig. 2. (**A**) Position of the front as function of exposure time, from the experiment of Fig. 1, D to F, as obtained by averaging the radius (half of the diameter) of the ring. (**B**) Front width from the same experiment.

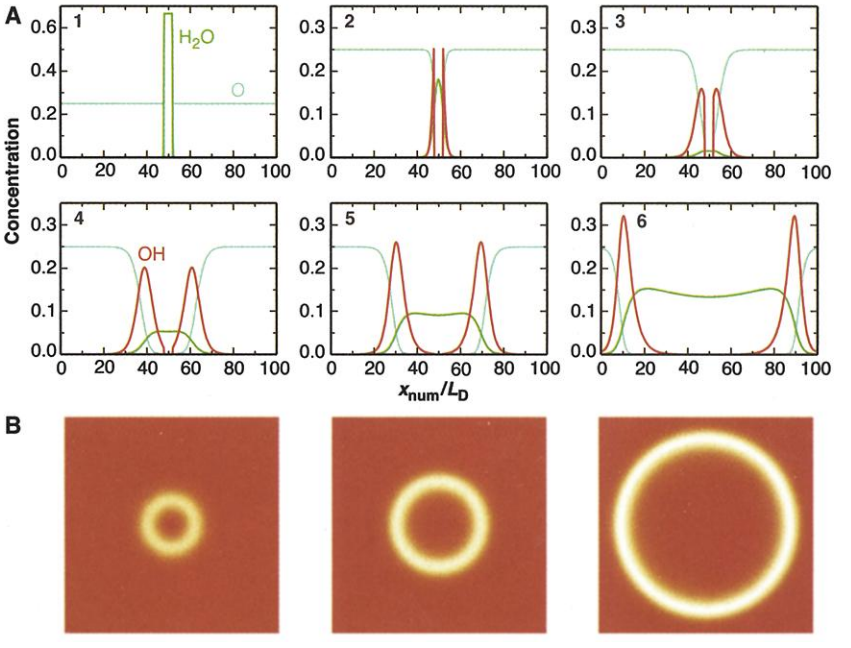

Fig. 3. Concentration profiles obtained by numerical integration of the 2D RD equations. The simulations are performed with a grid of 512 points by 512 points, and the length scale is given in units of the characteristic length $L_D = \sqrt{D/k_3}$. The system length was $L_S = 100\ L_D$, and the ratio of rate constants was $k_2/k_3 = 0.025$. (**A**) 1D cross sections. The first frame shows the initial configuration, an H_2O cluster on an otherwise O-covered surface (radius $R = 2.0\ L_D$), the second frame the formation of an OH zone at the O/H_2O interface. In the following frames, the front develops and expands radially. (**B**) 2D distribution of OH (bright ring). The frames are from the same time instants as frames 4 to 6 in (A).

rather narrow temperature ranges accessible in both studies. The rates themselves are in relatively good agreement; deviations only vary between factors of 8 and 2 between 133 and 144 K. DFT calculations for E_3 yielded a value of about 0.3 eV (*9, 14*), which is in the same range as the experimental data.

The diffusion coefficient of the adsorbed H_2O is the third kinetic parameter entering the RD-equations. According to DFT calculations (*9*) the activation energy E_D for diffusion on the bare Pt surface is very low, only 0.13 eV, which accounts for the high mobility of water at low temperatures, as also observed in previous experiments (*15*). However, the H_2O molecules also have to migrate across the OH zone to reach the O-covered area ahead of the front. This process is presumably connected with H transfer via $H_2O + OH \rightarrow OH + H_2O$, a fast process. Finally, the H_2O molecules have to diffuse into the O-covered region ahead of the front. Diffusion on the O-covered surface is affected by H-bond formation between H_2O and O (*6*), and should be slower than diffusion on the bare surface. The diffusion constant on the O-covered surface was determined by adsorption of low amounts of H_2O on the (2 × 2)O layer. STM images recorded afterwards showed small OH islands within the O layer, indicating a nucleation and growth process. Because OH itself is not mobile, the H_2O molecules must have diffused across the O layer until meeting each other or becoming attached to existing OH clusters. These trapped H_2O molecules are immobilized by H bonds, out of which state they react to give OH. Assuming homogeneous nucleation for defect-free terraces and a critical nucleus of one H_2O molecule, the diffusion coefficient could be obtained from the island density, the adsorption rate, and the total H_2O dose (*16*). The value of $D = 8.0 \times 10^{-12}$ cm^2 s^{-1} at 133 K corresponds, with the usual preexponential factor $D_0 = 10^{-3}$ cm^2 s^{-1}, to $E_D = 0.21$ eV. Because the diffusion of water on the O-covered surface limits the overall mobility of H_2O, these numbers are used in the numerical simulations.

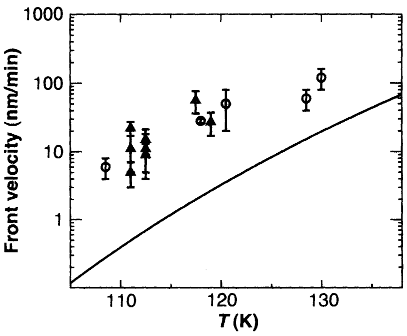

Fig. 4. Experimental front velocities (dots), compared with model predictions (line). The simulations were performed with the experimentally determined Arrhenius parameters for k_2, k_3, and D: $\nu_2 = 8.7 \times 10^6$ ML^{-1} s^{-1}, $E_2 = 0.27$ eV, $\nu_3 = 6.0 \times 10^6$ ML^{-1} s^{-1}, $E_3 = 0.20$ eV, $D_0 = 10^{-3}$ cm^2 s^{-1}, $E_D = 0.21$ eV.

The RD model, now containing only quantities derived from independent experiments, can now be used to make quantitative predictions about the front velocity and width as a function of temperature. For the front velocity (Fig. 4), the temperature dependence of the experimental data is nicely reproduced, but the absolute numbers are about one order of magnitude too low. This deviation is not considered to be a serious problem in view of the uncertainties of the values of the kinetic parameters. If, for example, E_2 is lowered from 0.27 to 0.22 eV, perfect agreement between experiment and theory results. The situation is less favorable for the front width. Whereas the experimental data show an increase with temperature, the simulations predict a slight decrease, and the absolute numbers in the simulations are up to three orders of magnitude higher. The agreement can be considerably improved, e.g., by increasing E_D from 0.21 eV to 0.27 eV, but then the agreement for the front velocity becomes worse. We could not adjust the Arrhenius parameters in the RD model in such a way as to achieve agreement simultaneously for both data sets.

We feel that, at this point, the limitations of the RD description are reached. The formation of adsorbate islands reflects interactions between the adsorbed species caused by H-bond formation. The macroscopic kinetic constants are therefore expected to depend on microscopic interaction parameters. In particular, the diffusion of adsorbed H_2O molecules must be affected by such interactions. The H_2O motion will be influenced by the local O coverage because of the H-bonding between the H_2O molecules and the O atoms, and there are strong attractions between the adsorbed H_2O molecules and adjacent water or OH particles that lead to clustering. Such microscopic effects may be systematically taken into account by constructing a microscopic model that is simulated by Monte Carlo (MC) techniques. So far, realistic MC simulations have not been accessible because of the large difference between the microscopic length scales and the diffusion length (*17*). Hybrid models combining local MC simulations with large-scale mean-field models (*18, 19*) or the use of finite elements with a locally coarse-grained dynamics (*20*) may solve this problem.

An alternative possibility would be to construct a mesoscopic model by coarse-graining the microscopic master equations. This type of model would describe the dynamics of continuous coverages and take into account internal fluctuations in a system of stochastic partial differential equations. Models of this type have been constructed previously to explore mechanisms for the formation of nanoscale patterns in reactive adsorbates with strong attractive lateral interactions (*21–23*). In the present case, features like strong attractive lateral interactions between adsorbed water molecules and surrounding H_2O and OH particles and the above-mentioned H exchange between a water molecule and an adjacent OH molecule can be systematically incorporated into a mesoscopic theory (*24*).

References and Notes

1. R. Imbihl and G. Ertl, *Chem. Rev.* **95**, 697 (1995).
2. H. H. Rotermund, W. Engel, M. Kordesch, G. Ertl, *Nature* **343**, 355 (1990).
3. A. S. Mikhailov, *Foundations of Synergetics I* (Springer, Berlin, 1994).
4. M. Eiswirth, G. Ertl, in *Chemical Waves and Patterns*, R. Kapral, K. Showalter, Eds. (Kluwer, Dordrecht, Netherlands, 1995), p. 447.
5. S. Völkening, K. Bedürftig, K. Jacobi, J. Wintterlin, G. Ertl, *Phys. Rev. Lett.* **83**, 2672 (1999).
6. K. Bedürftig *et al.*, *J. Chem. Phys.* **111**, 11147 (1999).
7. J. R. Creighton, J. M. White, *Surf. Sci.* **122**, L648 (1982).
8. A. Michaelides, P. Hu, *J. Chem. Phys.* **114**, 513 (2001).
9. ______, *J. Am. Chem. Soc.* **123**, 4235 (2001).
10. Step III was formulated on the basis of vibrational spectra (6), indicating that no H_2O remained after the reaction between H_2O and O. In contrast, Michaelides and Hu (8) found by DFT calculations that one of the two water molecules in step III remains intact and becomes incorporated into the OH phase. We will discuss this point in a forthcoming publication (*11*) where we also show that both reaction mechanisms lead to the same kinetic equations. This dispute has therefore no effect on the RD system and the following discussion.
11. C. Sachs, M. Hildebrand, J. Wintterlin, G. Ertl, in preparation.
12. J. R. Creighton, J. M. White, *Surf. Sci.* **136**, 449 (1984).
13. G. B. Fisher, B. A. Sexton, *Phys. Rev. Lett.* **44**, 683 (1980).
14. The second-order rate law for reaction III indicates that it consists of two steps where the reaction of one H_2O with O determines the rate. The value of 0.3 eV is for this step. Michaelides and Hu (9) find that a mechanism simultaneously involving both water molecules would cost an even lower energy, but such a process would represent a trimolecular step.
15. M. Morgenstern, J. Müller, T. Michely, G. Comsa, Z. *Phys. Chem.* **198**, 43 (1997).
16. Y. W. Mo, J. Kleiner, M. B. Webb, M. G. Lagally, *Phys. Rev. Lett.* **66**, 1998 (1991).
17. The diffusion length is the mean distance a molecule has to travel before it reacts.
18. M. Silverberg, A. Ben-Shaul, *J. Chem. Phys.* **87**, 3178 (1989).
19. M. Tammaro, M. Sabella, J. W. Evans, *J. Chem. Phys.* **103**, 10277 (1995).
20. V. B. Shenoy, R. V. Kukta, R. Phillips, *Phys. Rev. Lett.* **84**, 1491 (2000).
21. M. Hildebrand, A. S. Mikhailov, *J. Phys. Chem.* **100**, 19089 (1996).
22. ______, G. Ertl, *Phys. Rev. E* **58**, 5483 (1998).
23. ______, *Phys. Rev. Lett.* **81**, 2602 (1998).
24. Such a mesoscopic model is currently being developed by M. Hildebrand.
25. We gratefully acknowledge discussions with A. S. Mikhailov.

29 May 2001; accepted 19 July 2001